

# On the relationship between the wall-shear-stress and transient-growth disturbances in a laminar boundary layer

A. M. Naguib,<sup>1,a)</sup> J. F. Morrison,<sup>2</sup> and T. A. Zaki<sup>3</sup>

<sup>1</sup>Department of Mechanical Engineering, Michigan State University, East Lansing, Michigan 48824, USA

<sup>2</sup>Department of Aeronautics, Imperial College, London SW7 2AZ, United Kingdom

<sup>3</sup>Department of Mechanical Engineering, Imperial College, London SW7 2AZ, United Kingdom

(Received 30 July 2009; accepted 18 March 2010; published online 4 May 2010)

The present study is motivated by the development of wall-based flow-state estimators for feedback control of transient-growth disturbances in a laminar boundary layer. Such estimators have been successfully demonstrated in recent numerical studies, but they rely on information that, while available in simulations, is generally not accessible in the laboratory. Here, some physical aspects of transient-growth modes and their relationship to the unsteady wall shear stress are examined to guide the development of estimation methods that perform satisfactorily yet are practical to implement. The usefulness of the resulting physical understanding for flow estimation is *demonstrated* using a proper orthogonal decomposition mode estimator, applied to a direct numerical simulation of boundary layer transition beneath free-stream turbulence. The results shed light on the strengths and weaknesses of employing each of the streamwise and spanwise wall-shear-stress components in estimating the disturbance wall-normal velocity and vorticity fields. It is also found that the streamwise-elongated nature of transient-growth disturbances allows coarse sampling of the wall-shear-stress information used in the estimation without substantially deteriorating the estimation accuracy. This is particularly true for estimates based on the streamwise shear stress. © 2010 American Institute of Physics. [doi:10.1063/1.3415220]

## I. INTRODUCTION

### A. Bypass transition

This work is motivated by the overarching goal of implementing feedback control of transient growth in “bypass” boundary-layer transition. The latter refers to the transition scenario encountered in situations with strong background disturbances, such as that occurring beneath a turbulent free stream. Unlike the classical transition path, which begins with the exponential growth of two-dimensional, Tollmien–Schlichting (TS) waves, bypass transition is initiated with the *transient* growth of three-dimensional, streaky structures that are elongated, in the streamwise ( $x$ ) direction, and quasiperiodic in the spanwise ( $z$ ) direction. Early identification of these streaky structures is credited to Klebanoff,<sup>1</sup> who studied the growth of the associated disturbances in the wind tunnel beneath a free stream with varying levels of turbulence intensity (a short summary of Klebanoff’s experiment and key results can be found in Kendall<sup>2</sup>). Klebanoff (as well as the later investigations by Kendall,<sup>3</sup> Westin *et al.*,<sup>4</sup> and Matsubara and Alfredsson<sup>5</sup>) found the peak root-mean-square (rms) streamwise disturbance velocity  $u'_{\text{rms}}$  to grow in proportion to the square root of the streamwise distance (i.e., the streamwise energy of the streaks grows linearly, or algebraically, with downstream distance).

For sufficiently high Reynolds number, the streaks become strong enough to trigger nonlinear effects or secondary

instabilities, which in turn lead to formation of turbulent spots and subsequent transition to turbulence. Andersson *et al.*<sup>6</sup> found that a secondary inviscid instability of the streaks takes place when the streak amplitude exceeds 26% of the free-stream velocity. Recent direct numerical simulation (DNS) studies by Jacobs and Durbin<sup>7</sup> and Brandt *et al.*<sup>8</sup> enabled examination of the physical mechanisms leading to the streak breakup process. In addition, Zaki and Durbin<sup>9,10</sup> provided physical insight into the role of low- and high-frequency vortical disturbances in bypass transition, and the influence of pressure gradient on the amplification of streaks and subsequent transition to turbulence. For more details on bypass boundary-layer transition, the reader is referred to the recent review by Durbin and Wu.<sup>11</sup>

### B. Feedback control of bypass transition

In recent years, there has been substantial progress in the use of model-based, linear, control-theory approach for feedback flow control in computational studies, which is highlighted in the recent article by Kim and Bewley.<sup>12</sup> Successful examples of the use of this approach in the control of laminar-turbulent transition in wall-bounded flows include Hogberg and Henningson<sup>13</sup> who employed optimal control theory to control boundary layer transition, and Bewley and Liu<sup>14</sup> who utilized optimal and robust control theories to effectively reduce the disturbance response in a laminar, plane channel flow. The latter authors also demonstrated that modern control theory significantly outperformed the classical proportional-control-based methods.

<sup>a)</sup>Author to whom correspondence should be addressed. Telephone: (517) 432-1616. Fax: (517) 353-7179. Electronic mail: naguib@egr.msu.edu.

The success of the computational model-based control studies summarized above is yet to be realized in the laboratory. Experimental investigations of feedback control of transient growth in a laminar boundary layer have generally been rare, and mostly, *ad hoc*/intuition based. One of the notable experimental investigations is by Jacobson and Reynolds<sup>15</sup> who were successful in controlling a pair of streamwise vortices that was introduced in a controllable manner in the boundary layer. The authors employed a wall-flush, oscillating, cantilever-beam actuator downstream of the vortex pair in order to minimize the spanwise average and standard deviation of the wall-shear-stress downstream of the actuators. More recently, Lundell<sup>16</sup> demonstrated some heuristic control of transiently growing disturbances in a laminar boundary layer beneath a turbulent free stream. In his approach, a single hot-wire shear-stress sensor was employed in conjunction with a suction hole downstream of the sensor. The feedback control premise was quite simple: when the shear stress dropped below a given threshold, suction was applied at some time delay. Both the suction strength and time delay were determined through calibration.

## II. MOTIVATION AND OBJECTIVES

The premise of the feedback control of interest is based on detecting the streaky disturbances during the linear (transient) growth phase and applying an appropriate control action to nullify or weaken this growth. To achieve this, within the context of model-based control, models are required for estimating the disturbance velocity field from measurements at the surface beneath the boundary layer. The need to constrain the sensing to the surface is motivated by the desire to avoid intrusion into, and hence, modification of the flow. In addition, for the purpose of real-time implementation of the control, the estimation models must be efficient (i.e., low-order).

Given that the envisioned control targets the boundary layer disturbances during the linear growth stage, it is instructive to examine the equations governing linear growth of three-dimensional disturbances in a Blasius boundary layer. It is well known that, *in the parallel-mean-flow approximation*, these equations may be cast in terms of the wall-normal component of the disturbance velocity ( $v'$ ) and vorticity ( $\eta'$ ), the so-called Orr–Sommerfeld/Squire equations, as follows:

$$\left(\frac{\partial}{\partial t} + U\frac{\partial}{\partial x}\right)\Delta v' - \frac{d^2U}{dy^2}\frac{\partial v'}{\partial x} - \frac{1}{R}\Delta\Delta v' = 0, \quad (1)$$

$$\left(\frac{\partial}{\partial t} + U\frac{\partial}{\partial x}\right)\eta' - \frac{1}{R}\Delta\eta' = -\frac{dU}{dy}\frac{\partial v'}{\partial z}, \quad (2)$$

where  $U$  is the mean streamwise velocity of the base flow,  $R$  is the Reynolds number,  $\Delta$  is the Laplacian operator,  $t$  is time and  $x$ ,  $y$ , and  $z$  are the streamwise, wall-normal, and spanwise coordinates.

Inspection of Eq. (2) shows that  $v'$  acts as a forcing function of  $\eta'$ . Physically, this may be explained through the “lift-up” mechanism, an explanation of which was provided by rapid distortion theory (Ref. 17). The physical mecha-

nism, which was later described by Landahl,<sup>18</sup> is as follows:  $v'$  disturbances cause movement of fluid elements across the mean-velocity gradient  $dU/dy$ . As a result, low-speed fluid is pumped away from the wall, while high-speed fluid is moved toward the wall, creating spanwise variation in the streamwise velocity,  $\partial u/\partial z$ , at a given  $y$  which in turn gives rise to wall-normal vorticity. Alternatively, Butler and Farrell<sup>19</sup> view the physical mechanism of forcing as tilting of the spanwise vorticity of the mean flow into the wall-normal direction by  $\partial v'/\partial z$ .

In the context of transition beneath a turbulent free stream,  $\partial v'/\partial z$  on the right hand side of Eq. (2) may be interpreted as resulting from free-stream disturbances that are able to penetrate into the boundary layer. The subsequent response of  $\eta'$  to this forcing gives rise to the transient growth of  $u'$ , leading to the formation of the streaks. Zaki and Durbin<sup>9</sup> demonstrated exact resonance between  $v'$  and  $\eta'$  and showed that, because of “shear-sheltering” (also see Ref. 10 as well as Ref. 20), only long-wavelength free-stream disturbances are able to penetrate near the wall to excite the boundary layer. This provides one explanation of the elongated structure of the resulting streaks.

Based on the above discussion, it is apparent that, for control purposes, it would be fruitful to provide feedback information on  $v'$  and/or  $\eta'$  fields from surface measurements. Since the former is the cause of the latter, knowledge of  $v'$  might be advantageous in giving the controller an “early warning” of subsequent transient growth (i.e., feedforward information). On the other hand, since  $v'$  decays in proportion to  $y^2$ , while  $u'$  and  $w'$  decay in proportion to  $y$  as the wall is approached,  $v'$  may not be inherently as observable (i.e., detectable) from surface measurements as  $u'$  and  $w'$  (as well as  $\eta'$ , since  $\eta' = \partial u'/\partial z - \partial w'/\partial x$ ).

Recently, success in wall-based estimation of the flow field of transiently growing disturbances in a laminar channel flow was accomplished in the study of Hoepffner *et al.*<sup>21</sup> These authors used a Kalman-filter approach that coupled the Orr–Sommerfeld/Squire equations with DNS “measurements” of the wall shear stress and pressure. However, the method, akin to numerical studies in general, employs an approach in which surface measurements are utilized at full simulation resolution, and shear stress as well as pressure information at the same point on the wall is available simultaneously. Such methods, though elegant and feasible in simulations, cannot be implemented in the laboratory (and hence ultimately in applications), given the practical challenge of sensing different quantities at the same point, the limited number of sensors usable in practice, the actual temporal and spatial resolution of sensors, realizable sensor types, etc.

In the present study, physical insight is sought in the relationship between linear, transiently growing disturbances and the wall-shear-stress in a laminar boundary layer. Our goal is to capitalize on this insight to develop an understanding of the practical limitations on the estimation of the disturbance field from surface shear stress measurements. For the purposes of the study, a DNS of boundary layer transition beneath a turbulent free stream (Ref. 22) is used. A subset of this database is first analyzed using space-time correlations

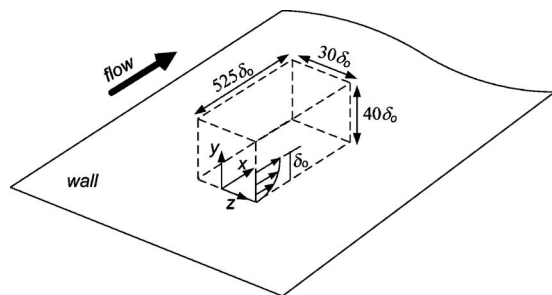


FIG. 1. Sketch of the computational domain.

to establish the spatiotemporal relationship between  $v'$  and  $\eta'$  disturbances on one hand, and the wall-shear-stress imprint on the other.

To draw links between the outcome of the correlation analysis and flow estimation, a proper-orthogonal-decomposition (POD)-based estimator is implemented. It is emphasized here that our selection of the POD estimator is motivated by the convenience of applying this estimator to the existing DNS. We do not necessarily advocate the use of POD framework for feedback control of transient growth, given some of its limitations that were recently brought into focus by Ilak and Rowley.<sup>23</sup> In particular, these authors demonstrated that some of the leading (most energetic) POD modes are not observable in laminar channel flow, and hence are inappropriate for modeling the input/output dynamics of transiently growing disturbances. Instead, they proposed the use of a “balanced” POD method (BPOD; introduced by Rowley<sup>24</sup>) in which the retained modes are the most observable and controllable. BPOD seems to provide a good alternative to, for example, using Orr–Sommerfeld/Squire modes for representing the flow, many of which were shown by Kim and Bewley<sup>12</sup> not to have a surface-shear-stress signature (i.e., to lack observability in wall-shear-based feedback). However, BPOD requires specific computations of the governing equations and their adjoint, and hence the method cannot be implemented on an existing database. Furthermore, the present investigation is concerned with understanding how physical and practical factors, that are independent of the specifics of the estimator, influence the accuracy of the estimation, rather than with developing an estimation method. To this end, we identify a significant, yet observable POD mode (one that can be estimated from wall shear stress with acceptable accuracy), and examine how the accuracy of estimating this mode would be altered by physical and practical limitations.

### III. DESCRIPTION OF THE DNS DATABASE

Figure 1 depicts the computational domain of the database employed here, which is generated using a simulation similar to that reported by Jacobs and Durbin,<sup>7</sup> and the associated coordinate system. The domain extends  $52.5\delta_0$ ,  $40\delta_0$ , and  $30\delta_0$  in the streamwise, wall-normal and spanwise directions, respectively, where  $\delta_0$  is the 99% boundary layer thickness at the upstream end of the domain (in contrast,  $\delta$  refers to the *local* boundary layer thickness). At the same streamwise location, the free-stream-turbulence intensity and

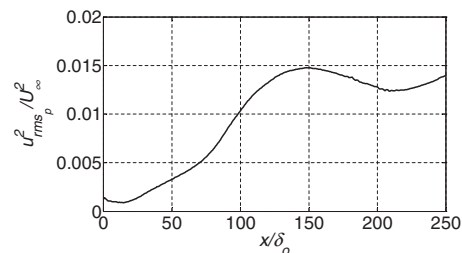


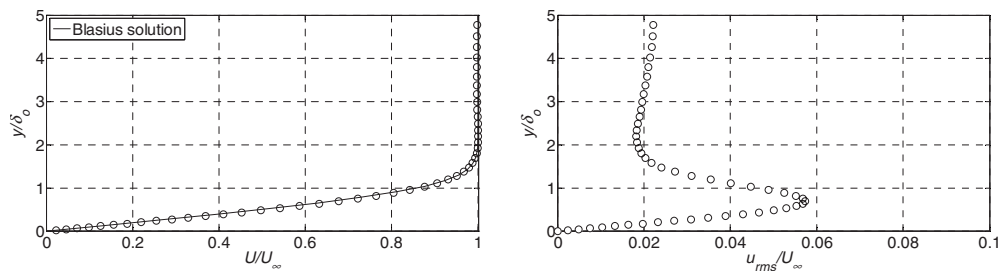
FIG. 2. Streamwise evolution of the peak streamwise energy.

integral length scale are 3.5% and  $1.8\delta_0$ , respectively. A uniformly distributed grid is used in the  $x$  and  $z$  directions to calculate the flow at 1793 and 193 nodes, respectively. On the other hand, the  $y$  grid is nonuniform and contains 193 points extending from the wall, where the resolution is finest, into the free stream, where the resolution is coarsest. A subset of the database containing  $897 \times 97 \times 97$  grid points in the  $x$ ,  $y$ , and  $z$  directions, respectively, at twice the spatial resolution of the original data set is employed in the present analysis. Thirty snapshots separated by a time delay of  $4\delta_0/U_{\infty}$  ( $U_{\infty}$  is the free-stream velocity) of the three velocity components ( $u$ ,  $v$  and  $w$  in  $x$ ,  $y$ , and  $z$  directions, respectively) are available at each grid point. Together, the available fields span a time duration that would be taken by a fluid particle to travel a distance of  $120\delta_0$  at the free-stream velocity.

To compute statistical quantities, averaging is performed in time as well as in the spanwise (homogeneous) direction. This results in a sample size of 2910 points for single-point statistics. Convergence tests at the streamwise location where the analysis is focused shows that mean-velocity values converge to better than 1%, while the fluctuating-velocity rms convergence uncertainty is less than 10%.

### IV. RESULTS

In order to identify the linear (algebraic) growth region within the flow domain, the maximum energy of the streamwise fluctuating velocity at each streamwise location is plotted versus the downstream distance in Fig. 2. The results depict a region of linear growth from  $x/\delta_0=20$  to 60. Although any location within this domain would be suitable for the present analysis, a location at  $x/\delta_0 \approx 50$  (49.8) is selected. The mean and rms streamwise velocity profiles at the selected location are shown in Fig. 3. The mean velocity profile compares well with the Blasius solution, providing confirmation of the absence of nonlinear effects at the selected  $x$  location. The 99% boundary layer thickness is approximately  $1.6\delta_0$ ; while the peak  $u'_{rms}$  fluctuation is about 5.8% of the free-stream velocity and is found at  $y/\delta_0=0.69$  (or  $y/\delta^*=1.23$ , where  $\delta^*$  is the displacement thickness, which compares closely with the experimental value of  $y/\delta^*=1.3$ , reported by Matsubara and Alfredsson<sup>5</sup> in the linear growth domain). The dominance of the streaky structure at this height is demonstrated in Fig. 4 where an instantaneous gray-shade contour map of  $u(x,z)$  is displayed at  $y/\delta_0=0.69$ . Dark and light regions that are quasiperiodic in the spanwise direction and elongated in the streamwise di-

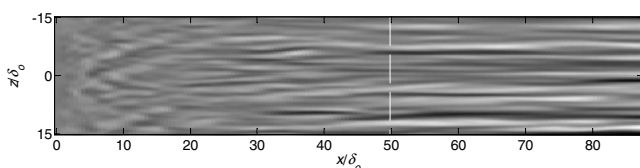
FIG. 3. Mean (left) and rms (right) streamwise velocity profiles at  $x/\delta_0=49.8$ .

rection reflect the streaky nature of the dominant  $u'$  disturbance. The characteristic spanwise wavelength of the streaks ( $\lambda_z$ ) is found to be approximately  $2.5\delta_0$  from the spanwise correlation function  $R_{u'u'}(\Delta z)$  at  $y/\delta_0=0.69$ : see Fig. 5. Thus, the computational domain contains roughly 12 streaks across the span.

### A. Physical argument

Linear, optimal growth theory (Refs. 19, 25, and 26) has shown that the disturbances whose energy grows the most over a particular time or streamwise distance in wall-bounded flows are associated with counter-rotating streamwise vortex pairs. Before examining if such vortex pairs are found in the simulated flow, it is helpful to consider *idealized* vortex pairs. This is shown in Fig. 6 along with the anticipated spanwise variation of the streamwise and spanwise wall shear stress,  $\tau'_x$  and  $\tau'_z$ , at the wall, as well as  $u'$ ,  $v'$ , and  $\eta'$ , at the height of the vortex centers above the wall ( $y_c$ ). As seen from the figure, the largest  $\tau'_z$  occurs directly beneath the vortex center. This coincides with the spanwise location of the peak  $\eta'$  magnitude at  $y=y_c$ . On the other hand the largest  $v'$  (and  $u'$ ) disturbance location will be in-between the vortex pair; i.e., offset from the peak  $\tau'_z$  position by  $\frac{1}{4}$  of the average streak spacing ( $\lambda_z$ ).

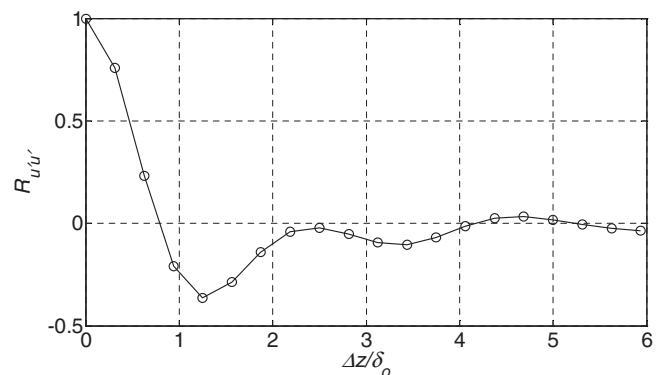
Although the model shown in Fig. 6 is idealized, and disturbances leading to optimal growth do not necessarily occur in the flow, two-point correlation results obtained from the DNS data are in fact consistent with the vortex-pair model. More specifically, at the streamwise location of the analysis,  $x/\delta_0 \approx 50$ , the largest correlation between  $\tau'_z$  and  $\eta'$  is found at a spanwise offset  $\Delta z=0$ ; and between  $\tau'_z$  and  $v'$  is seen at  $\Delta z=\lambda_z/4=0.62\delta_0$ . Furthermore, the actual instantaneous flow structure does exhibit association of the high/low-speed streaks with streamwise vorticity. This may be seen from the two contour plots shown in Fig. 7 representing typical snap shots of the streamwise vorticity  $\omega_x$  (de-

FIG. 4. Instantaneous snap shot of the streamwise velocity at  $y/\delta_0=0.69$ . Light and dark shades correspond to velocities above and below the local average velocity, respectively. The dashed line identifies the streamwise location of the present analysis.

picted using white contour lines) superposed on top of the streamwise-velocity disturbance field (shown using the gray-shades flooded color contour map) in the plane normal to the mean flow. Note that the shown vorticity contours are limited to those falling in the range  $|\omega_x \delta_0 / U_\infty| > 0.04$  (for reference the peak rms value of the streamwise vorticity at  $x/\delta_0 \approx 50$  inside the boundary layer is  $\omega_{x,rms} \delta_0 / U_\infty = 0.066$ ).

The top plot in Fig. 7 depicts an instant where counter-rotating vortex structures (the cores of which are identified as local peaks in the streamwise vorticity field that are numbered I, II, III, and IV) fall at the interface between low and high streamwise-velocity regions. The spanwise separation between vortices with the same sense of rotation is approximately equal to  $\lambda_z$  ( $2.5\delta_0$ ). However, even though the basic physical picture reflected in the top plot of Fig. 7 is qualitatively consistent with the essence of the idealized model depicted in Fig. 6, the organization of the actual flow structures is far from idealized. In particular, the actual vortex structures possess random size and strength, their cores are located at different heights above the wall, and their spanwise spacing is not regular. Moreover, as reflected in the bottom plot of Fig. 7, there are instants where a streamwise vortex structure appears in isolation. Such an isolated vortex is still associated with spanwise modulation of the streamwise velocity as seen from the gray-shade contours of the bottom plot in Fig. 7. Nevertheless, even in this case, the insight based on the vortex-pair model in relation to the spanwise offset between locations of high streamwise/spanwise wall shear stress and high  $u'$ ,  $v'$ , and  $\eta'$  disturbances, is useful.

A fuller picture of the correlation between  $\tau'_z(x \approx 50\delta_0, y=0, z, t)$  and  $\eta'(x \approx 50\delta_0, y, z+\Delta z, t+\Delta t)$ , de-

FIG. 5. Two-point spanwise correlation of the streamwise velocity at  $y/\delta_0=0.69$ .

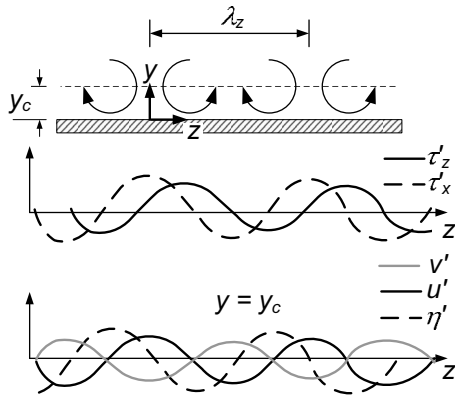


FIG. 6. A sketch of the streamwise vortex-pair model and associated *qualitative* variation in wall shear stress and disturbance field at  $y=y_c$  along the spanwise direction (mean flow direction is into the page, and the vertical scale is arbitrary).

noted by  $R_{\tau'_z \eta'}$ , for  $\Delta z=0$ , and  $R_{\tau'_z v'}$ , for  $\Delta z=0.62\delta_o$ , is shown in Fig. 8. The results are displayed in the form of a flooded gray-shade contour plot depicting the dependence of the correlation on the time offset ( $\Delta t$ ; abscissa) and the height above the wall (ordinate). Note that a positive  $\Delta t$  indicates a time lag of the disturbance field relative to the wall shear stress and vice versa. Inspection of Fig. 8 shows that the peak  $R_{\tau'_z v'}$  occurs at zero time delay at *all* heights in the boundary layer. On the other hand, at the top of the analysis domain, the peak in  $R_{\tau'_z \eta'}$  occurs at  $\Delta t=0$  and shifts progressively toward increasing values as the wall is approached. These observations lead to an interesting conclusion: whereas the occurrence of  $v'$  disturbance anywhere across the boundary layer is associated with an *immediate*  $\tau'_z$  signature,  $\eta'$  disturbances have a height-dependent phase lag relative to  $\tau'_z$ . Physically, these results may be interpreted as follows: an elongated streamwise vortex structure originating from the free-stream turbulence is able to penetrate the boundary layer, inducing  $v'$  disturbance and leaving an *instant*  $\tau'_z$  imprint beneath the vortex center. The  $\partial v'/\partial z$  associated with the vortex structure forces the  $\eta'$  field through the right hand side term of Eq. (2). The resulting  $\eta'$  response

is dictated by Eq. (2) and is such that the peak  $\eta'$  value is attained at progressively large time delay as the wall is approached.

Some understanding of the causes of the observed temporal relationship between the transient growth disturbances and the wall-shear-stress components may be gained through examination of the governing equations. First, consider the instantaneous link between  $v'$  and  $\tau'_z$ : If streamwise variation of  $u'$  is ignored relative to wall-normal and spanwise variation of  $v'$  and  $w'$ , respectively (as maybe justified on basis of the streamwise-elongated structure of the  $u'$  field; see Fig. 4), the mass conservation equation yields

$$\frac{\partial v'}{\partial y} + \frac{\partial w'}{\partial z} = 0. \quad (3)$$

Taking the derivative with respect to  $y$  and applying at the wall:

$$\left. \frac{\partial^2 v'}{\partial y^2} \right|_w = - \left. \frac{\partial}{\partial z} \frac{\partial w'}{\partial y} \right|_w = - \frac{1}{\mu} \frac{\partial}{\partial z} \tau'_z. \quad (4)$$

For a given spanwise wavenumber, say corresponding to the average streak spacing  $\lambda_z$ , the right hand side of Eq. (4) is proportional to  $\tau'_z/\lambda_z$ . Thus, one may write

$$\tau'_z \sim \lambda_z \left. \frac{\partial^2 v'}{\partial y^2} \right|_w. \quad (5)$$

Now consider a Taylor-series expansion of  $v'$  versus  $y$  starting from the wall. Both  $v'(y=0)$  and  $\partial v'/\partial y(y=0)$  vanish because of the no-slip condition. Hence,

$$v' = \frac{1}{2} \left. \frac{\partial^2 v'}{\partial y^2} \right|_w y^2 + O(y^3). \quad (6)$$

Equations (5) and (6) show that  $v'$  at a given height *near the wall* is proportional to  $\tau'_z/\lambda_z$ , consistent with the observed instantaneous dependence between the spanwise wall-shear stress and the wall-normal disturbance velocity. Physically, one may interpret this result to be caused by the non-penetration constraint imposed by the wall on  $v'$  disturbances. This constraint forces any  $v'$  disturbance to be turned along the span (in the elongated streamwise disturbance limit) causing a spanwise-shear-stress signature.

The high instantaneous correlation between  $v'$  and  $\tau'_z$  found here is consistent with the findings of Choi *et al.*<sup>27</sup> in the near-wall region of a turbulent channel flow. Employing the leading order term in the Taylor series expansion of  $v'(y)$ , but without the assumption of elongated streamwise disturbance as done above, Choi *et al.* could relate the near-wall  $v'$  to both the streamwise and spanwise wall shear-stress. However, because they found the correlation between the former and  $v'$  to be small, they only employed the spanwise wall shear stress in feedback control of drag in the channel flow. As will become clear from consideration of Fig. 10 below, the low correlation between  $v'$  and  $\tau'_x$  (which is also found here) is true when considering instantaneous dependence between those two quantities. However, with the incorporation of appropriate time delay, the correlation between  $v'$  and  $\tau'_x$  could be just as high as between  $v'$  and  $\tau'_z$  at the same time instant.

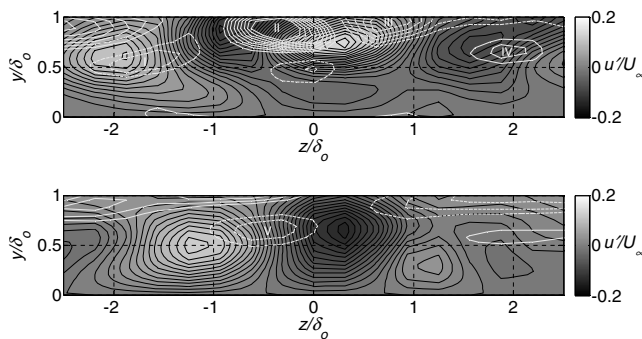


FIG. 7. Two snapshots of the instantaneous streamwise vorticity field (white contour lines) superposed on top of flooded gray-shade contour maps of the instantaneous streamwise disturbance velocity field. For clarity, shown vorticity contours are limited to the range  $|\omega_x \delta_o / U_\infty| > 0.04$  (in increments of 0.02) with solid and broken lines corresponding to positive and negative vorticity values, respectively. Top plot depicts four counter-rotating vortices (labeled I, II, III, and IV); bottom plot depicts an isolated vortex (labeled V).

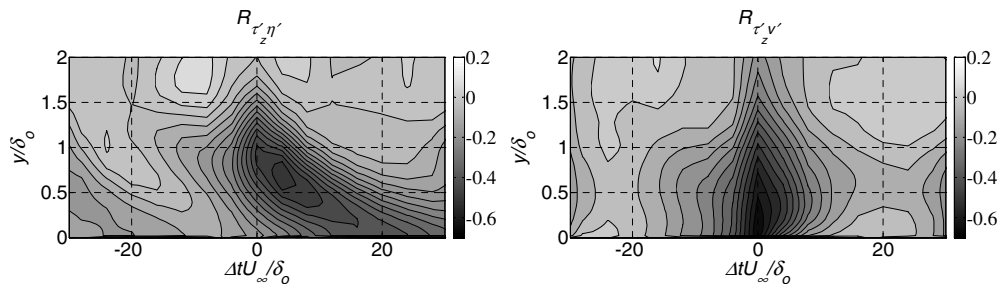


FIG. 8. Two-point correlation between  $\tau'_z$  and  $\eta'$  (left), and  $\tau'_z$  and  $v'$  (right) as a function of time delay (abscissa) and height above the wall (ordinate). Note that  $\tau'_z$  and  $v'$  information are taken from locations that are offset along the span by  $0.62\delta_0$ . No such offset is employed for the  $\tau'_z$  and  $\eta'$  correlation.

On the other hand, the lag of  $\eta'$  development relative to  $\tau'_z$  may be analyzed through examination of Eq. (2), which governs the response of  $\eta'$  to  $v'$  forcing. First, it is helpful to consider the characteristic diffusion time scale:  $t_v = \delta_0^2 / \nu$ ; which as a ratio to the convective time scale,  $\delta_0 / U_\infty$ , is the Reynolds number based on the boundary layer thickness at the inlet of the analysis domain  $t_v U_\infty / \delta_0 = U_\infty \delta_0 / \nu \approx 800$ . Noting that this is more than an order of magnitude larger than the largest observed correlation time delay ( $\Delta t U_\infty / \delta_0 \approx 20$  at the wall; see left plot in Fig. 8), it is clear that the latter is related to dynamics that are independent of viscous effects. Thus, ignoring the viscous term in Eq. (2), and assuming elongated streamwise disturbances (i.e.,  $\partial \eta' / \partial x \approx 0$ ), Eq. (2) reduces to

$$\frac{\partial \eta'}{\partial t} = - \frac{dU}{dy} \frac{\partial v'}{\partial z}, \quad (7)$$

the solution of which is

$$\eta' = - \frac{dU}{dy} \int \frac{\partial v'}{\partial z} dt + \text{IC}, \quad (8)$$

where IC is an initial condition. At a given  $y$  and for a disturbance of wavenumber  $2\pi/\lambda_z$ ,

$$\eta' \sim \frac{1}{\lambda_z} \int v' dt. \quad (9)$$

The above integral imposes a  $\pi/2$  phase delay of  $\eta'$  relative to  $v'$  at a given angular frequency  $\omega$ . The corresponding time delay is  $t_d = \pi/2\omega \sim 1/\omega$ . This suggests that the lower the frequency (or the larger the time scale) of the dominant disturbance at a given  $y$ , the longer is the time delay of  $\eta'$  relative to  $v'$  (and  $\tau'_z$ ). To determine the dominant disturbance time scale at different  $y$  locations, the autocorrelation of  $\eta'$  ( $R_{\eta' \eta'}$ ) is computed and the outcome is given in Fig. 9. The results show that the autocorrelation becomes broader as  $y$  decreases, which gives evidence that the time scale of the dominant  $\eta'$  disturbance does in fact become progressively larger as the wall is approached. This produces a corresponding larger time lag in the development of  $\eta'$  relative to  $v'$  (and  $\tau'_z$ ) with decreasing  $y$  (based on the above arguments), which is consistent with the behavior of  $R_{\tau'_z \eta'}$ .

Next, consider the correlation results involving the streamwise wall shear stress ( $\tau'_x$ ). The left plot in Fig. 10 depicts the correlation between  $\tau'_x$  and  $\eta'$ , for  $\Delta z = 0.62\delta_0$

(where the maximum correlation between these two quantities is found along the span) as well as between  $\tau'_x$  and  $v'$ , for  $\Delta z = 0$ . The axes are the same as in Fig. 8. Similar to the  $R_{\tau'_z \eta'}$  results, Fig. 10 shows a height-dependent phase difference between  $\tau'_x$  and  $\eta'$ . Unlike the  $R_{\tau'_z \eta'}$  results, however, where the spanwise shear stress signature is found to lead the wall-normal-vorticity field,  $\tau'_x$  lags behind the  $\eta'$  field. It is significant to note that this lag is quite large for the most “dangerous” disturbance occurring at the height of the peak  $u'_{\text{rms}}$  ( $y/\delta_0 = 0.69$ ). In particular, this delay is  $\Delta t U_\infty / \delta_0 \approx 12$ , which implies that at the time of measurement of  $\tau'_x$ , the associated  $\eta'$  disturbance at  $y/\delta_0 = 0.69$  would have traveled 7.5 boundary layer thicknesses (recall the local boundary layer thickness is approximately  $1.6\delta_0$ ; see Fig. 3) at the free-stream velocity, or approximately  $5\delta$  at the local mean velocity.

The evolution of  $\tau'_x$  signature is also found to lag behind that of  $v'$  disturbances. This is reflected in the results of  $R_{\tau'_x v'}$ , shown in the right half of Fig. 10. In particular, the correlation peak is found to occur at  $\Delta t U_\infty / \delta_0 \approx -16$  independent of height above the wall. This implies that by the time a  $\tau'_x$  signature is detected at the wall, the associated  $v'$  disturbance would have traveled approximately  $7\delta$  at the local mean velocity.

The observed delay between the occurrence of a  $v'$  disturbance in the flow and the generation of a related  $\tau'_x$  at the same  $x$  location is three-dimensional in nature, and can be identified through examination of the near-wall Taylor-series expansion of  $v'$  without ignoring the streamwise-dependence of the disturbance field. Referring to the work of Choi *et al.*,<sup>27</sup> who employed the series expansion in the near-wall region of a turbulent channel flow as discussed above,  $v'$  may be written as

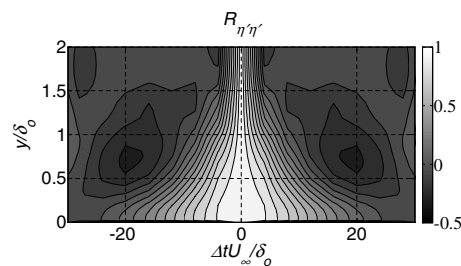


FIG. 9. Contour map of the autocorrelation of  $\eta'$  at different  $y$  locations.

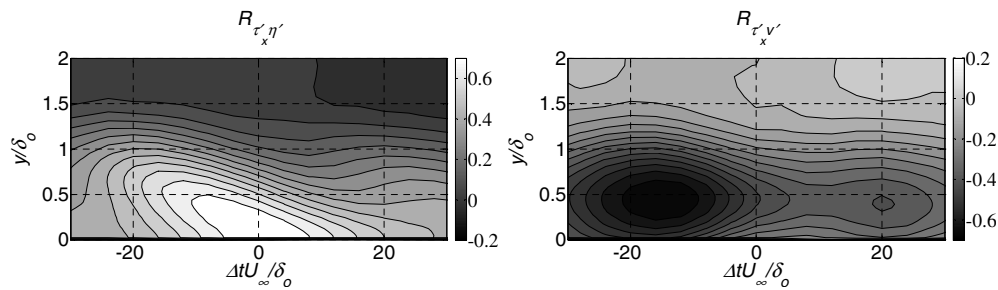


FIG. 10. Two-point correlation between  $\tau'_x$  and  $\eta'$  (left), and  $\tau'_x$  and  $v'$  (right) as a function of time delay (abscissa) and height above the wall (ordinate). Note that  $\tau'_x$  and  $\eta'$  information are taken from locations that are offset along the span by  $0.62\delta_0$ . No such offset is employed for the  $\tau'_x$  and  $v'$  correlation.

$$v' = -\frac{y^2}{2} \left[ \frac{\partial}{\partial x} \tau_x + \frac{\partial}{\partial z} \tau_z \right] + O(y^3). \quad (10)$$

It is evident from Eq. (10) that at a given height,  $v'$  is proportional to the streamwise derivative of the streamwise wall shear stress. This causes the phase of  $v'$  disturbance to lead that of the corresponding shear stress along the  $x$  coordinate. Employing a Taylor frozen-field argument, one can see how such a spatial phase lead in  $x$  would produce a similar phase offset in  $t$ . In fact, the same effect is embedded in the temporal derivative of Eq. (9) above. This clarifies the reason for the largest correlation between  $v'$  and  $\tau'_x$  taking place at a nonzero time delay, and that Choi *et al.* could have perhaps made use of  $\tau'_x$  in their feedback control of the turbulent channel flow had they considered the correlation with  $\tau'_x$  at nonzero time delay.

The above findings are quite significant in guiding the design of estimators based on the wall shear stress. In particular, they suggest that the use of  $\tau'_x$  (the easiest and more accurate of  $\tau'_x$  and  $\tau'_z$  to measure in practice) in a wall-based-estimation scheme would result in a time delay in the feedback of the flow state. A possible remedy to this issue in control-system implementation is to locate the actuators  $5-7\delta$  downstream of the wall-shear sensors such that by the time  $\tau'_x$  from a particular disturbance is detected, the disturbance will have convected downstream to the location where the actuators reside. However, the effectiveness of the control is likely to be affected by changes in the disturbance field caused by the following: (1) disturbance evolution as it convects downstream; and (2) the development of new disturbances over the streamwise stretch between the sensors and actuators through additional forcing of the boundary layer by free-stream turbulence.

In contrast,  $\tau'_z$  seems to have several advantages for flow-state estimation purposes. First,  $\tau'_z$  signature occurs at the same instant when the boundary layer is forced with  $v'$  disturbance. Second, this signature appears to take place  $4\delta_0/U_\infty$  ahead of the development of the strongest transient-growth disturbances at  $y/\delta_0=0.69$ , thus giving opportunity for the control system to respond.

In the following, the insights developed in this section are examined against the performance of a POD-based estimator.

## B. POD synthesis

Noteworthy POD studies of boundary layer transition include Rempfer and Fasel<sup>28</sup> and Rempfer<sup>29</sup> who applied POD to investigate boundary-layer transition initiated by TS waves. Chapman *et al.*<sup>30</sup> also conducted POD analysis on signals obtained from arrays of wall-shear-stress sensors in a laminar boundary layer undergoing cross-flow instability. Here, focus is on obtaining POD representation of free-stream-turbulence-induced transient-growth modes. To obtain this representation of  $v'(y, z, t)$  at the selected  $x$  location, the following synthesis equation is employed:<sup>31</sup>

$$v'(y, z, t) = \sum_{n=1}^N a_v^{(n)}(t) \phi_v^{(n)}(y, z), \quad (11)$$

where  $\phi_v^{(n)}$  is the  $n$ th POD eigenfunction or mode of the  $v'$  field,  $a_v^{(n)}$  is the corresponding expansion coefficient and  $N$  is the total number of POD modes. The POD modes are determined empirically from the snapshots of the  $v'$  field at the  $x$  location of interest, and they form a complete set of basis functions [i.e., any of the instantaneous realizations used in obtaining the POD modes is exactly recoverable using Eq. (11)]. Note that the analysis is carried out for the scalar field of the wall-normal velocity component rather than the velocity vector field. This is done since the latter is dominated by  $u'$  (the strongest of the three velocity components) and hence the associated POD modes would not be the most efficient in capturing  $v'$ . Similarly, only the wall-normal vorticity component  $\eta'$  of the vorticity vector field is considered in the POD analysis. Furthermore, for simplicity, this paper focuses on the estimation of the two-dimensional  $v'$  and  $\eta'$  field at a fixed  $x$  location.

The number of POD modes equals the number of grid points in the  $y$ - $z$  plane of the analysis; therefore, Eq. (11) does not immediately lead to low-order representation of the velocity field. However, because the POD procedure maximizes the projection of the fields' energy onto the empirical modes, in an average sense, Eq. (11) converges quickly and only a few modes are typically needed for satisfactory representation of the instantaneous field. This is particularly true for flows dominated by organized motions, or coherent structures, as in the current case.

Because the transitional boundary layer considered here

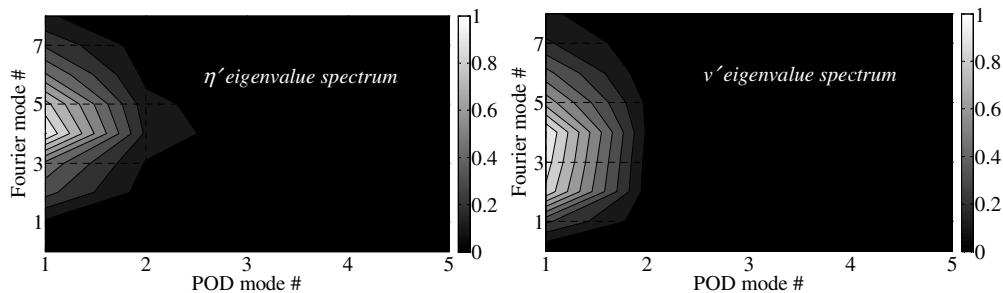


FIG. 11. Contour plot of the POD eigenvalue spectrum for  $\eta'$  (left) and  $v'$  (right) showing the fluctuation energy distribution among POD (abscissa) and Fourier (ordinate) mode pairs.

is homogeneous in the spanwise direction, the POD eigenfunctions are sinusoidal, or Fourier modes, along the span. Thus, one only needs to carry out the POD analysis along the  $y$  direction after Fourier transforming the field in the span. The one-dimensional POD expansion for a given spanwise wavenumber,  $k_z$ , may then be written as

$$V_{k_z}(y, t) = \sum_{n=1}^N A_{v, k_z}^{(n)}(t) \Phi_{v, k_z}^{(n)}(y), \tag{12}$$

where  $V_{k_z}$  is the Fourier transform of  $v'$  in the spanwise direction evaluated at wavenumber  $k_z$ . The coefficients  $A_{v, k_z}^{(n)}$  are obtained from an inner product of  $V_{k_z}$  with the eigenfunctions using

$$A_{v, k_z}^{(n)}(t) = \int_0^{y_o} V_{k_z}(y, t) \Phi_{v, k_z}^{(n)*}(y) dy. \tag{13}$$

Note that superscript  $*$  indicates complex conjugation and that the integration limits in Eq. (13) assume that the POD domain extends from the wall up to a height  $y_o$  above the wall. Once the  $A_{v, k_z}^{(n)}$  are obtained for a particular realization, a truncated version of Eq. (12) can be used to obtain a low-order representation of  $V_{k_z}$ . Subsequently, inverse Fourier transformation of the latter along the span can be used to synthesize the  $v'$  field from the POD and Fourier modes. Of course, if the field is purely harmonic, or quasiperiodic in the spanwise direction, only one or a few Fourier modes need to be kept in the inverse transformation, and further reduction in the order of the velocity-field representation is obtained.

To focus the analysis on the region that is most significant to transient growth, the POD domain is taken from the wall up to  $y/\delta_o=1$ . This choice of the analysis domain produces a more compact POD representation of the disturbance field than one that extends to the edge of the boundary layer.

Referring to Fig. 3, it is evident that the selected domain is focused around the region where  $u'_{rms}$  peaks. The POD modes are obtained from the solution of the following eigenvalue problem:

$$\sum_{j=1}^{ny} W_j \langle V_{k_z}(l, t) V_{k_z}^*(j, t) \rangle \Phi_{v, k_z}^{(n)}(j) = \Lambda_{k_z}^{(n)} \Phi_{v, k_z}^{(n)}(l), \tag{14}$$

$$l = 0, 1, \dots, ny$$

where  $\langle \rangle$  denotes averaging over time and  $3 \times 32$ -point spanwise records,  $W_j$  are integration factors,  $j$  and  $l$  are integers representing  $y$  node locations,  $ny$  is the number of  $y$  nodes within the selected analysis domain and  $\Lambda_{k_z}^{(n)}$  are the eigenvalues. Equation (14) yields a set of linear, algebraic equations with coefficient matrix of size  $ny \times ny$ , which is solved to obtain the eigenvalues and eigenvectors (POD modes).

Figure 11 displays a flooded gray-shade contour plot of the two-dimensional, eigenvalue spectrum of  $\eta'$  and  $v'$  POD modes. Specifically, the plot gives the magnitude of the eigenvalue for every Fourier and POD mode pair. Since the total fluctuation energy is the sum of all eigenvalues [divided by the number of points used in the spanwise fast Fourier transform (FFT)], Fig. 11 gives information concerning how the energy is distributed among different modes. Note that the eigenvalues have been normalized by the magnitude of their largest, i.e., the contour values range from zero to one. Because a 32-point FFT is used to obtain the Fourier modes, mode 0 is the spanwise-uniform mode (which was subtracted in the analysis), mode 1 has 32 points per cycle, mode 2 has 16 points per cycle, and so on.

Figure 11 shows that for both  $\eta'$  and  $v'$ , the largest energy is associated with Fourier mode number 4, corresponding to eight points per cycle, or a wavelength of  $2.5\delta_o$ .

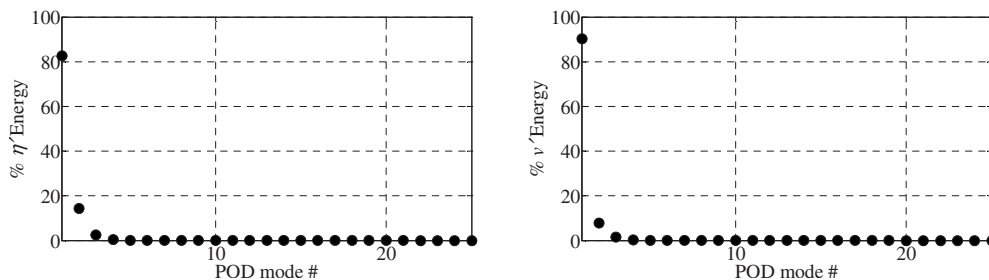


FIG. 12. Percentage fluctuation energy captured by individual POD modes:  $\eta'$  (left) and  $v'$  (right).

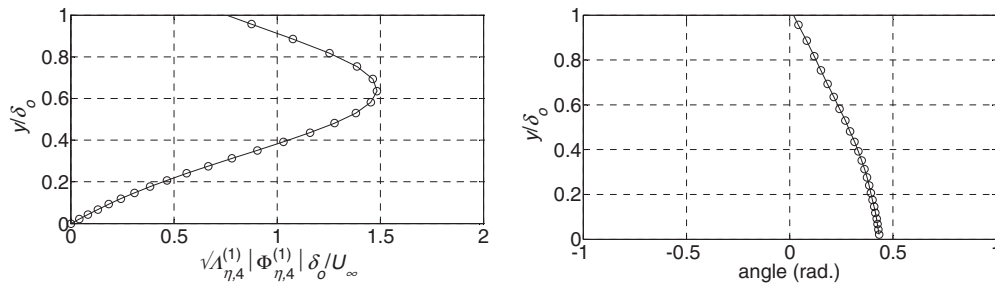


FIG. 13. Magnitude (left) and phase (right) of the leading  $\eta'$  POD mode/Fourier mode 4 (note the magnitude is multiplied by the square root of the eigenvalue).

This is the same as the average streak spacing obtained from the spanwise correlation results in Fig. 5. In addition, it appears that most of the energy is concentrated within Fourier modes 1 through 7 (out of 16 independent modes). In comparison, out of 25 POD modes, only two modes are needed to capture practically all the energy. The extremely fast POD convergence can be seen more clearly by summing the eigenvalues over all wavenumbers and plotting the results versus the POD mode number in Fig. 12. As seen from the figure, more than 80% of  $\eta'$  and  $v'$  fluctuation energy is captured by mode 1, with practically all of the remaining energy captured by mode 2. For reference, the magnitude and phase of the leading POD modes of  $\eta'$  and  $v'$  may be seen in Figs. 13 and 14 for the wavenumber corresponding to the streak spacing (Fourier mode 4).

### C. Wall-based estimation of POD mode coefficients

The combined linear stochastic estimation and POD (LSE/POD) method introduced by Bonnet *et al.*<sup>33</sup> is used to estimate the POD mode coefficients from the wall-shear-stress information. Specifically, when using the spanwise surface shear stress to estimate  $A_{\eta,kz}^{(n)}$  and  $A_{v,kz}^{(n)}$ , the following linear relations are employed:

$$\tilde{A}_{\eta,kz}^{(n)}(t) = K_{\eta,kz}^{(n)} T_{z,kz}(t), \quad (15)$$

$$\tilde{A}_{v,kz}^{(n)}(t) = K_{v,kz}^{(n)} T_{z,kz}(t), \quad (16)$$

where  $\sim$  indicates an estimated value,  $T_{z,kz}$  is the spanwise Fourier transform of the spanwise wall shear stress, and  $K_{\eta,kz}^{(n)}$  and  $K_{v,kz}^{(n)}$  are the estimation coefficients of the  $\eta'$  and  $v'$  POD coefficients, respectively.  $K_{\eta,kz}^{(n)}$  and  $K_{v,kz}^{(n)}$  are calculated such that the mean-squared error between the true and esti-

mated values of  $A_{\eta,kz}^{(n)}(t)$  and  $A_{v,kz}^{(n)}(t)$  is minimized. The procedure leads to the following forms for the LSE coefficients:

$$K_{\eta,kz}^{(n)} = \frac{\overline{A_{\eta,kz}^{(n)} T_{z,kz}}}{\overline{T_{z,kz} T_{z,kz}}}, \quad (17)$$

$$K_{v,kz}^{(n)} = \frac{\overline{A_{v,kz}^{(n)} T_{z,kz}}}{\overline{T_{z,kz} T_{z,kz}}}, \quad (18)$$

where the overbar denotes averaging in time and along the span. For estimation based on the streamwise shear stress,  $T_{z,kz}$  is replaced by  $T_{x,kz}$  in the above equations.

Figure 15 shows a comparison between the estimated and actual POD coefficients for the leading POD mode and Fourier mode 4 at different times. The estimated data are based on the spanwise wall shear stress. Overall, there is good correspondence between the true and estimated values for the estimation of the  $v'$  mode coefficient. In contrast, the estimate of  $A_{\eta,kz}^{(n)}(t)$  is not as good, where the estimate of both the real and imaginary component show significant deviation from the actual value. The quality of the estimation is assessed by computing a coherence coefficient ( $\Gamma$ ) between the actual and estimated mode coefficients using the following expression:

$$\Gamma = \frac{\overline{|A_{\eta,kz}^{(n)} \tilde{A}_{\eta,kz}^{*(n)}|}}{[\overline{A_{\eta,kz}^{(n)} A_{\eta,kz}^{*(n)}}]^{1/2} [\overline{\tilde{A}_{\eta,kz}^{(n)} \tilde{A}_{\eta,kz}^{*(n)}}]^{1/2}}, \quad (19)$$

where  $\|$  denotes the magnitude of the complex number and superscript  $*$  indicates complex conjugation. For the results shown in Fig. 15 the coherence values are 0.63 and 0.79 for the estimation of  $A_{\eta,4}^{(1)}$  and  $A_{v,4}^{(1)}$ , respectively. Since a perfect estimate would yield a coherence value of unity, the esti-

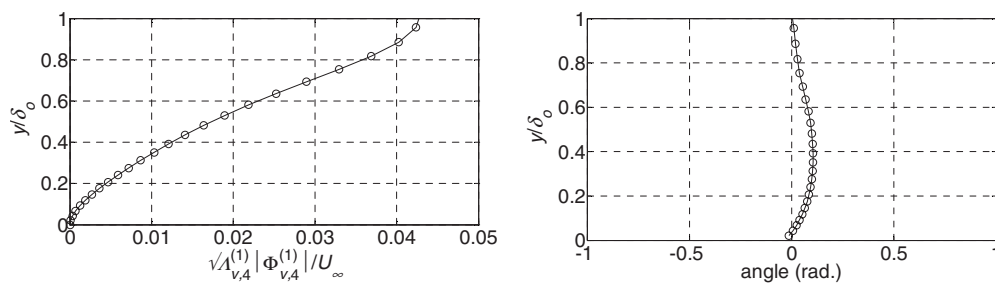


FIG. 14. Magnitude (left) and phase (right) of the leading  $v'$  POD mode/Fourier mode 4 (note the magnitude is multiplied by the square root of the eigenvalue).

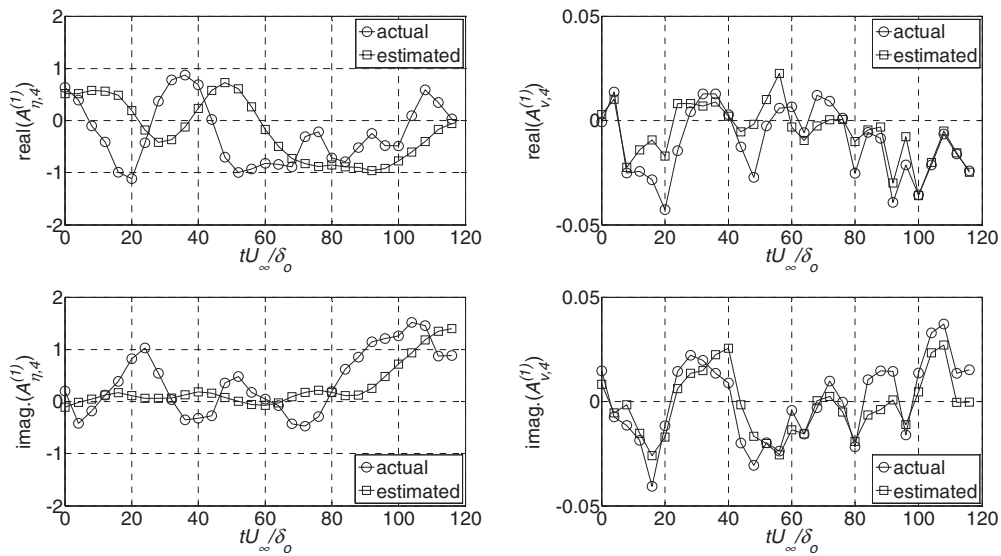


FIG. 15. Comparison between the actual and estimated coefficients of POD mode 1 and Fourier mode 4 for  $\eta'$  (left) and  $v'$  (right) fields: real (top) and imaginary (bottom) values.

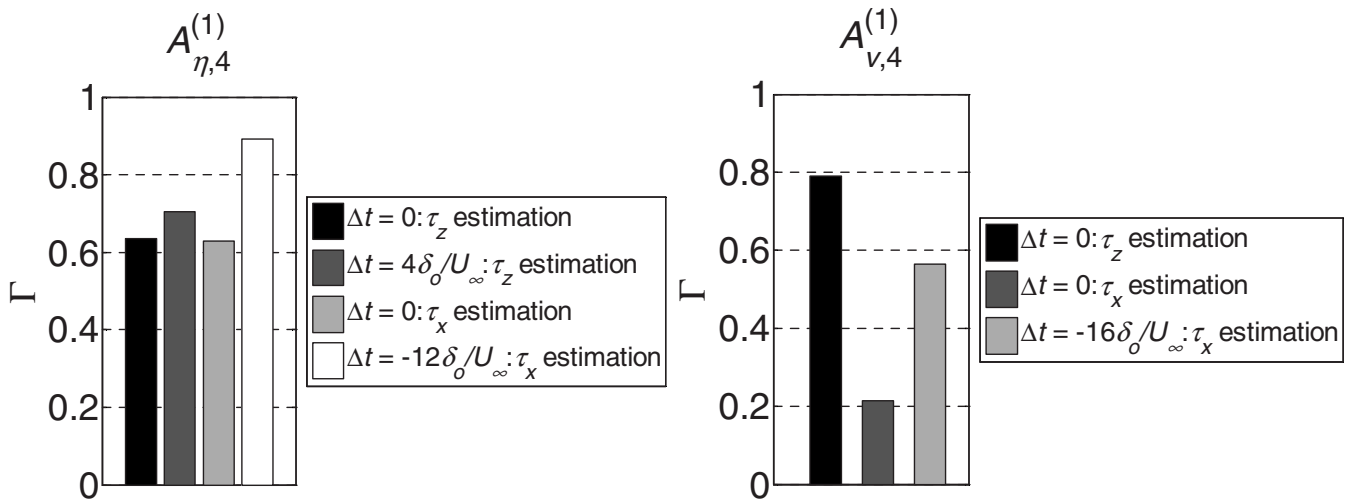


FIG. 16. Effect of the wall-shear-stress component and time delay used in the estimation of  $A_{\eta,4}^{(1)}$  (left) and  $A_{v,4}^{(1)}$  (right) on the estimation accuracy.

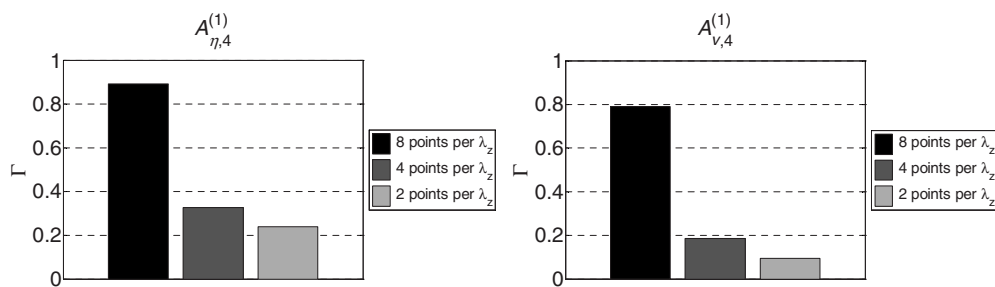


FIG. 17. Effect of sampling resolution of the wall shear stress on the estimation accuracy of  $A_{\eta,4}^{(1)}$  (left) and  $A_{v,4}^{(1)}$  (right).

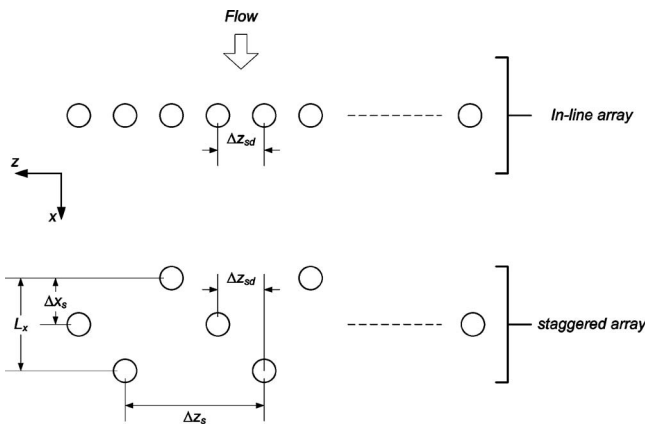


FIG. 18. Schematic drawing depicting in-line (top) and staggered (bottom) configurations for sampling the wall-shear-stress information.

mates of the POD coefficients in Fig. 15 may be considered as “noisy measurements” with the measurement of the  $\eta'$  POD coefficient being more noisy than that of  $v'$ .

An improvement upon the accuracy of the estimates in Fig. 15 can be accomplished through the utilization of a Kalman filter that incorporates a dynamical model of the POD mode coefficients [e.g., based on Galerkin projection of Eqs. (1) and (2) onto the POD modes]. An example of such an approach applied to the Lorenz model and wall-mounted cube in a channel flow is discussed by Mokhasi *et al.*<sup>34</sup> This, however, is outside the scope of the present study.

The correlation analysis in Sec. IV A provides a guide to achieving better estimation accuracy of the POD coefficient of  $\eta'$ . In particular, the analysis shows that the highest correlation between  $\eta'$  and  $\tau'_z$  occurs at time offset of  $\Delta t = 4\delta_o/U_\infty$  and between  $\eta'$  (at  $y/\delta_o = 0.69$  where peak  $u'_{\text{rms}}$  is found) and  $\tau'_x$  occurs at time offset of  $\Delta t = -12\delta_o/U_\infty$ . This suggests that  $\tau'_z$  values observed at time  $t$  yield the best estimate of  $\eta'$  at time  $t + 4\delta_o/U_\infty$ . Similarly, a  $\tau'_x$ -based estimate of the strongest  $\eta'$  disturbances will be most accurate for disturbances that occur  $12\delta_o/U_\infty$  in time ahead of the wall-shear values used in the estimation.

The results in Fig. 15 show the POD coefficients found at the same time instant as the wall-shear values used in the estimation. Similar results but incorporating the time offsets discussed above are obtained for estimations based on the streamwise as well as the spanwise wall shear stress. The corresponding  $\Gamma$  values of these estimates are depicted in

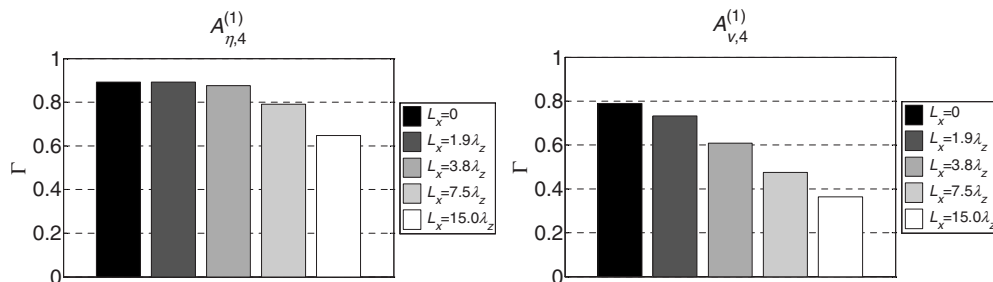


FIG. 19. Effect of the streamwise extent of staggered sampling of the wall-shear-stress information on the estimation accuracy of  $A_{\eta,4}^{(1)}$  (left) and  $A_{v,4}^{(1)}$  (right). Results shown are for a three-row staggered configuration.

Fig. 16. For reference,  $\Gamma$  values for  $\Delta t = 0$  are also included in the figure. Figure 16 contains two plots depicting results for the estimation of  $A_{\eta,4}^{(1)}$  (left plot) and  $A_{v,4}^{(1)}$  (right plot). Focusing on the former, it is seen that consistent with the correlation results, the estimation of  $A_{\eta,4}^{(1)}$  using  $\tau'_z$  does improve when  $A_{\eta,4}^{(1)}$  is estimated  $4\delta_o/U_\infty$  into the future. The improvement increases the coherence value from 0.63 (at zero time offset) to 0.7. The most accurate estimate of  $A_{\eta,4}^{(1)}$  is accomplished based on the *streamwise* wall shear stress and time delay of  $12\delta_o/U_\infty$ . The corresponding coherence between the estimate and true values is 0.9. On the other hand, the most accurate estimate of  $A_{v,4}^{(1)}$  is based on concurrent values of the *spanwise* wall shear stress. Overall, these results show that the accuracy of flow estimation is consistent with the physical understanding gained through inspection of the two-point correlation.

## D. Effect of sensing density on estimation accuracy

A matter that is of importance to practical implementation of estimators is whether wall-sensor arrays can be packed with sufficient density in actual experiments to achieve the same estimation accuracy found in testing/developing the estimator using numerical simulations. Generally, sensor density is limited by the physical sensor size, intersensor interference, and the economy of covering large surfaces (such as the wing of an airplane) by densely packed sensor arrays. To further illustrate the point,  $A_{\eta,4}^{(1)}$  and  $A_{v,4}^{(1)}$  are estimated using wall-shear-stress information sampled at spanwise spacing coarser than the resolution of the DNS database. At full resolution, eight wall-shear-stress data points fit within the average streak spacing ( $\lambda_z$ ). Estimations based on a coarser sampling rate of four and two data points per  $\lambda_z$  are conducted, and the accuracy of the results is compared in Fig. 17 to the full-resolution estimate. Note that no anti-alias filtering of the wall-shear signature is implemented before downsampling the data along the span. This is done in order to mimic wall-shear sampling in practice where such filtering is not possible. Also note that here, and for the remainder of the paper,  $A_{\eta,4}^{(1)}$  estimation is based on the streamwise wall shear stress and time delay of  $12\delta_o/U_\infty$ , while the estimation of  $A_{v,4}^{(1)}$  employs the spanwise wall shear stress and zero time delay. As found from Fig. 16, these particular combinations of the shear stress component and time delay yield the best estimate of the POD coefficients. Inspection of Fig. 17 shows

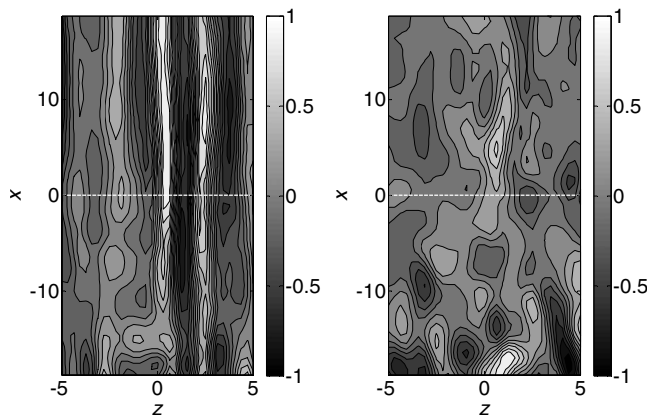


FIG. 20. Sample instantaneous maps of the streamwise (left) and spanwise (right) wall shear stress. The gray-shade bar on the right indicates the shear stress value normalized by the peak value within the domain displayed. The extent of the domain is  $15\lambda_z$  along  $x$  and  $4\lambda_z$  along  $z$ , and the broken white line identifies the streamwise location of the analysis.

that substantial drop in the accuracy of the estimation is produced as a result of downsampling below eight points per streak spacing. The coherence of the estimation decreases to less than 0.4 for  $A_{\eta,4}^{(1)}$  and 0.2 for  $A_{v,4}^{(1)}$ . This result underscores the fact that, whereas an estimation method may perform satisfactorily in a numerical simulation, practical matters such as limited sensor density, could lead to unsatisfactory performance in the laboratory, and ultimately in applications.

Illustrated in Fig. 18 is an alternate sensor configuration that can help address the sensor density requirements of boundary-layer, transient-growth estimators in practice. At the top of figure, the configuration that has been used for the estimation results hitherto (referred to as “in-line” array) is displayed. The alternate “staggered” array geometry (shown at the bottom of Fig. 18) involves distributing the same number of sensors as the in-line configuration over a number of rows covering a streamwise fetch of  $L_x$ , while maintaining the same desired spanwise spacing  $\Delta z_{sd}$  between successive sensors. In turn, this increases the spanwise spacing between the sensors ( $\Delta z_s$ ) at a given  $x$  location by a factor equal to the number of rows in the stagger. For example, the sensor array shown at the bottom of Fig. 18 is staggered over three rows, allowing the intersensor spacing at a given  $x$  to triple. This staggered geometry is motivated by the physical understanding that the transient growth modes are elongated along the streamwise direction. Thus, offsetting the sensors along  $x$ ,

within reasonable limits, should result in a nonsubstantial change in the wall-shear-stress signature. The configuration is particularly helpful when the desired intersensor spacing is limited by the physical size of the sensor.

Figure 19 depicts the coherence of  $A_{\eta,4}^{(1)}$  and  $A_{v,4}^{(1)}$  estimates using a three-row staggered array configuration covering different streamwise fetch lengths. The case of  $L_x=0$  represents the best estimate using an in-line array. As observed in Fig. 19, the coherence of the  $A_{\eta,4}^{(1)}$  estimate is barely affected by staggering the sensor array over a streamwise length of as much as approximately  $4\lambda_z$ . On the other hand, a noticeable decline in the accuracy of the  $A_{v,4}^{(1)}$  estimate with the increase in the streamwise extent of the staggered array is evident. However, the estimate retains substantial coherence (of approximately 0.7 or more) up to  $L_x \approx 2\lambda_z$ . The coherence of both  $A_{\eta,4}^{(1)}$  and  $A_{v,4}^{(1)}$  estimates drops to a similar value of approximately 0.6 for  $L_x \approx 15\lambda_z$  and  $4\lambda_z$ , respectively. The fair insensitivity of the  $A_{\eta,4}^{(1)}$  estimate to staggering of the sensor array over a relatively large streamwise domain stems from the fact that the estimate is based on  $\tau'_x$ , which is associated with structures that are highly elongated in the  $x$  direction. This may be seen from the left plot in Fig. 20. Similar elongated features are not found in the  $\tau'_z$  field, which is employed in estimating  $A_{v,4}^{(1)}$ ; see the right plot in Fig. 20.

The results presented in Fig. 19 correspond to a three-row array stagger. If it is desired to increase the sensor spacing  $\Delta z_s$  (e.g., for sensors that are big in size), the number of rows in the stagger need to be increased (in general,  $\Delta z_s = \text{number of rows in stagger} \times \Delta z_{sd}$ ). To investigate the effect of increasing the number of rows in the stagger, estimation of the POD mode coefficients is done for staggered-array configuration containing three, five and nine rows. The corresponding  $L_x$  values are  $0.94\lambda_z$ ,  $1.88\lambda_z$ , and  $2.82\lambda_z$ . The coherence of the resulting estimates is given in Fig. 21, where the case corresponding to one row of sensors represents the best estimate based on an in-line array. It is noted here that for the nine-row stagger, the sensor spacing at a fixed  $x$  location  $\Delta z_s$  increases to  $1.125\lambda_z$ , in comparison to  $0.125\lambda_z$  for the in-line sensor geometry. Notwithstanding this almost order of magnitude increase in sensor spacing, the accuracy of estimating  $A_{\eta,4}^{(1)}$  barely changes. The coherence of the estimate of  $A_{v,4}^{(1)}$ , on the other hand, decreases but remains above 0.6.

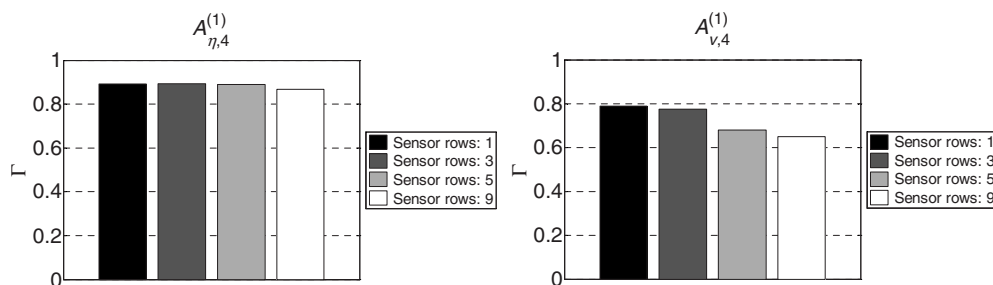


FIG. 21. Effect of the number of rows in staggered sampling of the wall-shear information on the estimation accuracy of  $A_{\eta,4}^{(1)}$  (left) and  $A_{v,4}^{(1)}$  (right).

## V. CONCLUSIONS

The present study employs a DNS database of a laminar boundary layer subjected to free-stream turbulence to investigate the relationship between transient-growth disturbances in the boundary layer and the wall-shear-stress signature. The study is motivated by understanding this relationship in order to guide the development of accurate, yet practically implementable, estimation models of the disturbance field based on surface-shear-stress information for feedback control of boundary layer transition. To this end, two-point correlations between the wall shear stress and the wall-normal velocity ( $v'$ ) and vorticity ( $\eta'$ ) are examined. The results of this examination are employed to arrive at the best performance of an estimator based on linear stochastic estimation/proper orthogonal decomposition (LSE/POD). It is found that the most accurate estimate of the coefficient of the leading POD modes (which capture more than 80% of the energy of each of  $v'$  and  $\eta'$ ) is achieved when using the spanwise wall shear stress ( $\tau'_z$ ) to estimate  $v'$  and the streamwise wall shear stress ( $\tau'_x$ ) to estimate  $\eta'$ . An interesting finding is that estimates based on  $\tau'_z$  are in phase with or leading the evolution of the disturbances in the flow. On the other hand,  $\tau'_x$ -based estimates lag behind the disturbance field. This finding has important ramifications regarding the decision of whether to select  $\tau'_z$  or  $\tau'_x$  for estimation as well as on the relative placement of sensors and actuators in feedback control implementation. Finally, the sensitivity of the estimator to the utilization of coarsely sampled wall-shear-stress information is examined. The outcome indicates that a staggered wall-shear-stress sensing configuration that makes use of the streamwise-elongated nature of the transient-growth modes allows for an appreciable increase in sensor spacing (up to approximately twice the average spanwise spacing of the transient-growth streaks) without substantial reduction in the estimation accuracy. This finding is particularly true for estimations based on the streamwise wall shear stress.

## ACKNOWLEDGMENTS

We are indebted to EPSRC (U.K.) for financial support, grant reference (Grant No. GR/S82947).

- <sup>1</sup>P. S. Kelbanoff, "Effects of free-stream turbulence on a laminar boundary layer," *Bull. Am. Phys. Soc.* **10**, 1323 (1971).
- <sup>2</sup>J. M. Kendall, "Experiments on boundary-layer receptivity to free-stream turbulence," AIAA Paper No. 98-0530, 1998.
- <sup>3</sup>J. M. Kendall, "Experimental study of disturbances produced in a pre-transitional laminar boundary layer by weak free-stream turbulence," AIAA Paper No. 85-1695, 1985.
- <sup>4</sup>K. J. A. Westin, A. V. Boiko, B. G. B. Klingmann, V. V. Kozlov, and P. H. Alfredsson, "Experiments in a boundary layer subjected to free stream turbulence. Part 1. Boundary layer structure and receptivity," *J. Fluid Mech.* **281**, 193 (1994).
- <sup>5</sup>M. Matsubara and P. H. Alfredsson, "Disturbance growth in boundary layers subjected to free-stream turbulence," *J. Fluid Mech.* **430**, 149 (2001).
- <sup>6</sup>P. Andersson, L. Brandt, A. Bottaro, and D. S. Henningson, "On the breakdown of boundary layer streaks," *J. Fluid Mech.* **428**, 29 (2001).

- <sup>7</sup>R. G. Jacobs and P. A. Durbin, "Simulations of bypass transition," *J. Fluid Mech.* **428**, 185 (2001).
- <sup>8</sup>L. Brandt, C. Cossu, J.-M. Chomaz, P. Huerre, and D. S. Henningson, "On the convectively unstable nature of optimal streaks in boundary layers," *J. Fluid Mech.* **485**, 221 (2003).
- <sup>9</sup>T. A. Zaki and P. A. Durbin, "Mode interaction and the bypass route to transition," *J. Fluid Mech.* **531**, 85 (2005).
- <sup>10</sup>T. A. Zaki and P. A. Durbin, "Continuous mode transition and the effects of pressure gradient," *J. Fluid Mech.* **563**, 357 (2006).
- <sup>11</sup>P. Durbin and X. Wu, "Transition beneath vortical disturbances," *Annu. Rev. Fluid Mech.* **39**, 107 (2007).
- <sup>12</sup>J. Kim and T. R. Bewley, "A linear systems approach to flow control," *Annu. Rev. Fluid Mech.* **39**, 383 (2007).
- <sup>13</sup>M. Högberg and D. S. Henningson, "Linear optimal control applied to instabilities in spatially developing boundary layers," *J. Fluid Mech.* **470**, 151 (2002).
- <sup>14</sup>T. R. Bewley and S. Liu, "Optimal and robust control and estimation of linear paths to transition," *J. Fluid Mech.* **365**, 305 (1998).
- <sup>15</sup>S. A. Jacobson and W. C. Reynolds, "Active control of streamwise vortices and streaks in boundary layers," *J. Fluid Mech.* **360**, 179 (1998).
- <sup>16</sup>F. Lundell, "Reactive control of transition induced by free-stream turbulence: An experimental demonstration," *J. Fluid Mech.* **585**, 41 (2007).
- <sup>17</sup>O. M. Phillips, "Shear-flow turbulence," *Annu. Rev. Fluid Mech.* **1**, 245 (1969).
- <sup>18</sup>M. T. Landahl, "A note on an algebraic instability of inviscid parallel shear flows," *J. Fluid Mech.* **98**, 243 (1980).
- <sup>19</sup>K. M. Butler and B. F. Farrell, "Three-dimensional optimal perturbations in viscous shear flow," *Phys. Fluids A* **4**, 1637 (1992).
- <sup>20</sup>T. A. Zaki and S. Saha, "On shear sheltering and the structure of vortical modes in single- and two-fluid boundary layers," *J. Fluid Mech.* **626**, 111 (2009).
- <sup>21</sup>J. Hoepffner, M. Chevalier, T. R. Bewley, and D. S. Henningson, "State estimation in wall-bounded flow systems. Part 1. Perturbed laminar flows," *J. Fluid Mech.* **534**, 263 (2005).
- <sup>22</sup>T. A. Zaki, Ph.D. thesis, Stanford University, 2005.
- <sup>23</sup>M. Ilak and C. W. Rowley, "Modeling of transitional channel flow using balanced proper orthogonal decomposition," *Phys. Fluids* **20**, 034103 (2008).
- <sup>24</sup>C. W. Rowley, "Model reduction for fluids, using balanced proper orthogonal decomposition," *Int. J. Bifurcation Chaos Appl. Sci. Eng.* **15**, 997 (2005).
- <sup>25</sup>P. Andersson, M. Berggren, and D. S. Henningson, "Optimal disturbances and bypass transition in boundary layers," *Phys. Fluids* **11**, 134 (1999).
- <sup>26</sup>P. Luchini, "Reynolds-number-independent instability of the boundary layer over a flat surface: Optimal perturbations," *J. Fluid Mech.* **404**, 289 (2000).
- <sup>27</sup>H. Choi, P. Moin, and J. Kim, "Active turbulence control for drag reduction in wall-bounded flows," *J. Fluid Mech.* **262**, 75 (1994).
- <sup>28</sup>D. Rempfer and H. F. Fasel, "Evolution of three-dimensional coherent structures in a flat-plate boundary layer," *J. Fluid Mech.* **260**, 351 (1994).
- <sup>29</sup>D. Rempfer, "On the structure of dynamical systems describing the evolution of coherent structures in a convective boundary layer," *Phys. Fluids* **6**, 1402 (1994).
- <sup>30</sup>K. Chapman, M. Reibert, W. Saric, and M. Glauser, "Boundary-layer transition detection and structure identification through surface shear stress measurements," Proceedings of the 36th Aerospace Sciences Meeting and Exhibit, Reno, NV, 12–15 January 1998, AIAA Paper No. 98-0782.
- <sup>31</sup>For theoretical background and details of the POD analysis, the reader is referred to Holmes *et al.* (Ref. 32). Also, for brevity, only  $v'$  equations are shown. The corresponding equations pertaining to  $\eta'$  are similar.
- <sup>32</sup>P. Holmes, J. L. Lumley, and G. Berkooz, *Turbulence, Coherent Structures, Dynamical Systems and Symmetry* (Cambridge University Press, Great Britain, 1996).
- <sup>33</sup>J. P. Bonnet, D. R. Cole, J. Delville, M. N. Glauser, and L. S. Ukeiley, "Stochastic estimation and proper orthogonal decomposition: Complementary techniques for identifying structure," *Exp. Fluids* **17**, 307 (1994).
- <sup>34</sup>P. Mokhasi, D. Rempfer, and S. Kandala, "Predictive flow-field estimation," *Physica D* **238**, 290 (2009).